Effects of Geometry of Wings Submerged in Turbulent Bluff-Body Wake

Zhehong Zhang[1], Zhijin Wang[2] and Ismet Gursul[3]
Department of Mechanical Engineering,
University of Bath, Bath, BA2 7AY, UK

Abstract

The effects of aspect ratio, sweep angle, and the leading-edge geometry of wings placed in a turbulent wake were investigated in wind tunnel experiments at a chord Reynolds number of 10^5. The post-stall lift enhancement due to the leading-edge vortex formation was studied at optimal locations in the wake. The effects of the strength of leading-edge vortices, ratio of spanwise length scale of incident vortex to wing-span, and degree of two-dimensionality of wake-wing interaction were studied. The competition between the effects of the spanwise length scale of the incident wake and the strength of the leading-edge vortices determined the optimal aspect ratio, which was found to be around 4. Increasing the sweep angle decreased the mean lift due to the decreased two-dimensionality of the vortex formation. Airfoils with sharp leading-edge produced the strongest leading-edge vortices, but further away from the wing surface, resulting in lower maximum lift. Relative to the performance in undisturbed freestream, the increases in the stall angle and maximum lift coefficient were not significantly affected the leading-edge shape.

1 Ph.D. Student, Department of Mechanical Engineering.
2 Senior Lecturer, Department of Mechanical Engineering. Senior Member AIAA.
3 Professor, Department of Mechanical Engineering. Associate Fellow AIAA.

Nomenclature

AR = aspect ratio

C_L = wing lift coefficient

C_{vv} = two-point cross-correlation of cross-stream velocity fluctuations

c = chord length, m

f = fundamental frequency of vortex shedding, Hz

H = vortex generator (bluff body) thickness, m

L = spanwise length scale of the incident vortices, m

Re_c = Reynolds number based on the chord length

Re_H = Reynolds number based on the bluff body thickness

sAR = semi-aspect ratio

T = period, s

t = time, s

t/c = thickness-to-chord ratio

U_∞ = freestream velocity, m/s

U = time-averaged streamwise velocity, m/s

u' = fluctuating streamwise velocity, m/s

$\langle u \rangle$ = phase-averaged streamwise velocity, m/s

V = time-averaged cross-stream velocity, m/s

v = fluctuating cross-stream velocity, m/s

$\langle v \rangle$ = phase-averaged cross-stream velocity, m/s

x = streamwise coordinate

y = cross-stream coordinate

x_{LE} = streamwise coordinate of the wing leading-edge

y_{LE} = cross-stream coordinate of the wing leading-edge

z = spanwise coordinate

α = angle of attack, ^{o}

Γ = circulation, m^2s^{-1}

Λ = sweep angle, ^{o}

λ_∞ = wavelength of the incident vortex street, m

ω = spanwise vorticity, s^{-1}

I. Introduction

Wings operating in the wakes of upstream bodies are commonly found in aerodynamics. Unsteady flows and large-scale vortices present in the wakes are expected to influence the forces and moments acting on wings submerged in wakes. Some examples of wings submerged in wakes include tandem wings such as canard-wing configurations [1], formation flight [2], flight refuelling, aircraft in ship airwakes during carrier take-off or landing [3], wings downstream of propellers, rotor blades in turbomachinery [4], and wind turbines. Vortex-wing interactions also exist for tandem flapping wings [5].

The interaction of coherent vortices with the wing may induce flow separation, shedding of secondary vortices (leading-edge vortices) [6], laminar separation bubbles, and transitional flows [7]. Fluctuating surface pressure fields and unsteady forces have been the focus of several investigations (for example, [8,9]). For many engineering applications, the time-averaged aerodynamic forces and moments acting on wings submerged in wakes have been of great interest. Coherent vortices in the wakes may induce flow separation from the leading-edge, and therefore affect the time-averaged lift of the downstream wings. Depending on the offset distance of the wing from the wake centerline, a decreased [10,11] or unaffected lift slope [12] in the pre-stall regime are observed. It is worth noting that large-scale vortices in the wakes produce similar effects as the elevated freestream turbulence (up to 15% in intensity), which contain large-scale vortical structures [13-16].

For a wing submerged in wakes, the delay of the stall angle is observed for all cases, regardless of the offset distance of the wing. The stall angle of attack can reach 20 degrees for a wing with NACA0012 cross-section, resulting in an increase of 64% in the maximum lift coefficient compared to the undisturbed freestream. The optimal wing location that provides the largest mean lift increase is located at the edge of the wake (see Figure 1(a)), rather than at the centerline [17]. The lift enhancement in the post-stall regime has some similarities with those found for tandem wings [18,19]. For wings submerged in wakes, Zhang *et al*. [17] have shown that the wake vortices periodically induce leading-edge vortices, similar to dynamic stall vortices on pitching or plunging wings [20] and in unsteady freestream [21,22]. Interestingly, the optimal location is at the edge of the wake where the amplitude of the flow oscillations is smaller than those at the wake centerline. Small-amplitude excitation provides larger vorticity flux into the leading-edge vortices compared to the wing located at the wake centerline where the wing experiences long periods of attached and completely separated flows with no roll-up. This results in stronger leading-edge vortices at the optimal location.

Zhang *et al*. [17] have concluded that there are two important parameters that affect the lift enhancement: the strength of the leading-edge vortices and the spanwise length-scale of the incident wake. The strength of the leading-edge vortices shed from the wing depends on the frequency and the wavelength of the incident vortex street (see Figure 1(a)). For the best case observed, the ratio of the wavelength of the incident vortex street to the chord length of the wing was $\lambda_\infty/c \approx 1.6$. The second important parameter, which is the spanwise length scale of the incident vortices, is close to the wavelength of the incident vortex street ($L \approx \lambda_\infty$) for a wake Reynolds number in the range of 10,000 to 50,000. This implies that the leading-edge vortex shedding will not be perfectly synchronized in the spanwise direction. Hence, the ratio of the spanwise length scale of the incident vortices in the wake to the wing-span may be an important parameter. With the decreasing aspect ratio of the wing, we may expect more synchronized flow separation in the spanwise direction, and a more beneficial effect of the wake on the time-averaged lift. The first objective of this article is to investigate the effect of wing aspect ratio when the wings are submerged in the same wake with a known spanwise length scale.

The second objective is to understand the effect of the wing leading-edge sweep. It is well known that the nature of the leading-edge separation and the vortex formation may change, depending on the sweep angle. For example, plunging swept wings may exhibit leading-edge vortices that are mostly in the spanwise direction [23,24]. For gust encounters by swept wings, leading-edge vortex shedding may be parallel to the incident gust or parallel to the leading-edge of the wing, depending on the angle of attack [25]. As the incident gust interacts with the wing gradually, starting near the root and moving to the tip region last, the gust forces are smaller in magnitude but act for longer durations [26]. Based on this evidence we may expect an influence of the wing sweep angle for the wings submerged in the wakes. The wavelength of the incident vortex street is of the same order as the chord length ($\lambda_\infty/c \approx 1.6$) in our case. The relatively large sweep angle causes decreased two-dimensionality of the leading-edge vortex formation, effectively introducing a phase delay in the spanwise direction.

Lastly, the third objective is to investigate the effect of the leading-edge geometry as this will directly affect the separation, vorticity flux, and the strength of the leading-edge vortices when the wings are submerged in the same wake. For this purpose, we investigated different airfoil cross-sections, including a flat-plate with a sharp leading-edge, at the same Reynolds number in the same wake. It is known that a sharp-leading edge can produce stronger leading-edge vortices, but they are formed a little further away from the surface, compared to

a rounded leading-edge for harmonic plunge oscillations of airfoils [27] and low-aspect-ratio wings [28]. Hence, their contribution to the increased lift force might be different.

In this article, we investigate the effects of aspect ratio, leading-edge sweep angle, and the leading-edge geometry for wings placed in a turbulent wake. The lift force and velocity field measurements were carried out in a wind tunnel at a Reynolds number based on the chord length of $Re_c = 10^5$. The mechanism of leading-edge vortex formation, shedding and convection as well as the strength of the vortices were studied. The effects of the wing geometry on the lift enhancement are discussed.

II. Methodology

A. Experimental setup

The experiments were carried out in a low-speed, closed-loop, open-jet wind tunnel located at the University of Bath. It has a circular working section with a diameter of 0.76 m and a length of 1.1 m. The wind tunnel has a maximum operating speed of 30 m/s and a freestream turbulence intensity of 0.1% at the maximum operational speed [29]. The schematic of the wing in the wakes is sketched in Figure 1(a) and the detailed experimental setup is shown in Figure 1(b). Since both airfoil and finite wing geometries are tested in the present investigation, two wake generators with different spans of 400 mm and 600 mm are used. For the wing testing, the span of the wake generator was equal to 600 mm, corresponding to the distance between the two end-plates shown in Figure 1(b). For the airfoil testing, the top end-plate was lowered to near the wing-tip, effectively producing nominally two-dimensional flow. In this case, another identical wake generator with a shorter span (400 mm) was manufactured. The wake generators are D-shaped cylinders with the same thickness of H = 50 mm, and have an elliptical leading-edge and a blunt rear-end. Two end-plates are used to generate nominally two-dimensional wakes.

Figure 1(c) shows four finite wings tested in addition to the airfoil geometry, all with the NACA0012 profile. The finite wings have semi-aspect ratios of sAR = 0.5, 1, 2, and 4 (equivalent to the full aspect ratios of 1, 2, 4, and 8). Figure 1(d) shows the two swept wings of sweep angles of 20^o and 40^o in addition to the unswept wing, all with the same semi-aspect ratio of sAR = 4 and the NACA0012 profile. Shown in Figure 1(e) are the three different wing profiles tested, namely NACA0012, NACA0006 and flat plate with thickness-to-chord ratio t/c=0.12 and chamfer angle of 30^o at both the leading edge and trailing edge, all with sAR=4 and zero sweep angle. All wings are of chord length c = 100 mm. All measurements are

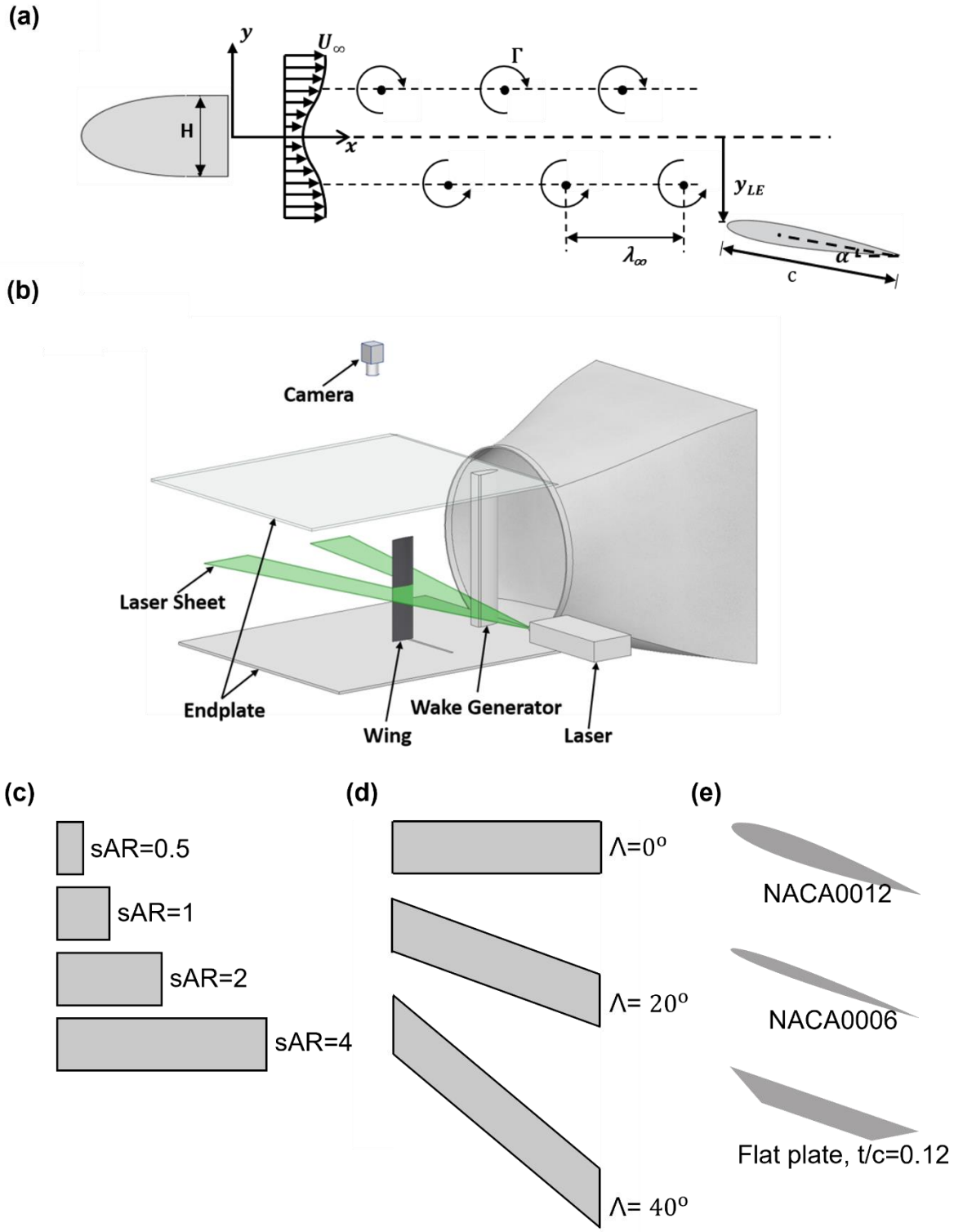

Figure 1: (a) Schematic of the wing in the wake of a bluff body; (b) schematic of the experimental setup and the PIV measurements; (c) wings with varying aspect ratio and the NACA0012 cross-section; (d) wings with varying sweep angle, *sAR*=4 and the NACA0012 profile; (e) wings with varying profile, *sAR*=4 and zero sweep angle.

conducted at a constant freestream velocity of U_∞ = 15 m/s, which corresponds to a Reynolds number based on the chord length of Re_c = 100,000. The Reynolds number of the wake based on the bluff body thickness H is Re_H= 50,000. The maximum blockage ratio in the experiments is 4.25%. In all measurements, the wing is located at a fixed streamwise location x_{LE}/c =3, but at varying cross-stream offset y_{LE}/c from the wake centreline.

B. Force measurements

The wing is mounted vertically to a two-axis traverse via an aluminium binocular strain gauge force balance. The lift force signal from the force balance is amplified through an AD624 instrumentation amplifier and logged to a personal computer via an NI6009 DAQ at a sampling rate of 5 kHz. In each measurement, the force signal is recorded for 20 s which is sufficiently long for the mean and the RMS of the signal to reach a steady-state value with variation less than 0.5%. The uncertainty in the force measurement is estimated to be δC_L = ±0.03. Uncertainties are calculated based on the methods of Moffat [30].

C. PIV measurements

The Particle Image Velocimetry (PIV) measurements have been carried out using a TSI 2D-PIV system. The measurement plane is selected to be parallel to the freestream in the streamwise direction and at halfway across the semi-span. The flow is seeded with olive oil droplets of 1μm in diameter produced by a TSI 9307-6 atomizer. The seeding particles at the desired measurement plane are illuminated by a NewWave Solo 120-15 Hz double-pulse laser system. The laser has a maximum laser energy output of 120 mJ per pulse. The laser pulse and an 8 MP Powerview Plus CCD camera are synchronized via the LaserPulse 610036 synchroniser. The commercial software package Insight 4G and a Hart cross-correlation algorithm are used to analyse the images. In the image processing, an interrogation window size of 32 × 32 pixels is selected, resulting in an effective grid size of approximately 2 mm which corresponds to a spatial resolution of approximately 0.02c. For each run, 2,000 instantaneous flow fields are captured at a rate of 1 Hz. The uncertainty for velocity measurements is within 2.2% of the freestream velocity U_∞, and the uncertainties of vorticity and circulation are estimated as 4%.

D. Phase-averaged velocity

In order to investigate the interaction of the quasi-periodic wake with the wing, a phase-averaging method based on the Proper Orthogonal Decomposition (POD) has been used. The POD method is one of the many modal analysis tools used in fluid mechanics for reduced-order modelling of coherent structures. The POD decomposes fluctuating flow fields as

$$\vec{u}(\vec{x},t) = \vec{U}(\vec{x}) + \vec{u}'(\vec{x},t) = \vec{U}(\vec{x}) + \sum_{1}^{N} a_n(t)\vec{\Phi}_n(\vec{x}) \tag{1}$$

where U and u' denote the mean and fluctuating velocity components. In this equation, $\vec{\Phi}_n$ and a_n are the POD modes and corresponding mode coefficients. The POD modes $\vec{\Phi}_n$ are obtained from the eigen-modes of the eigenvalue problem:

$$C\vec{\Phi}_n = \lambda_n\vec{\Phi}_n \text{ with } C_{i,j} = \overline{\vec{u}'(\vec{x}_i,t)\cdot\vec{u}'(\vec{x}_j,t)} \tag{2}$$

Oudheusden *et al*. [31] proposed a global and robust phase angle identification method using the first order approximation of the POD decomposition with the first two POD modes:

$$\begin{aligned} \vec{u}_{LOM} &= \vec{U}(\vec{x}) + a_1(\varphi)\vec{\Phi}_1(x) + a_2(\varphi)\vec{\Phi}_2(x) \\ a_1 &= \sqrt{2\lambda_1}\sin(\varphi) \quad a_2 = \sqrt{2\lambda_2}\cos(\varphi) \end{aligned} \tag{3}$$

where φ is the vortex shedding phase angle, assumed to increase linearly with time according to $\frac{d\varphi}{dt} = 2\pi f$, where f is the fundamental frequency of vortex shedding. In the present study, Oudheusden *et al.*'s method is used to identify the phase angle of the wake in each PIV image. For this method to work, the first two POD modes need to be dominant. Therefore, a smaller field of view upstream of the wing containing only the wake is selected to identify the phase information of the wake flow. For all PIV measurements, the energy captured by the first two modes is between 57% to 61%, slightly less than the 61% to 66% reported by Oudheusden *et al.* [31]. With the phase information of vortex shedding determined for each PIV image pairs, the PIV data are then phase-sorted in a bin size of ±10° to obtain the phase-averaged representation of the flow field. For each phase (e.g., φ = 0°), there are over 105 (about 5.25% of total captured snapshots) instantaneous flow fields that fall in a phase bin size of ±10°, and these snapshots are averaged to obtain the phase-averaged flow fields. We tried ±2°, ±5°and ±10° bin sizes. The difference between ±5°and ±10° bin size is minimal.

III. Results and Discussion

In order to characterize the incident wake in the absence of the wing, we show the contours of the normalized time-averaged streamwise velocity and the normalized rms value of the cross-stream velocity fluctuations in Figure 2(a) and 2(b) respectively. The optimal locations for various aspect ratio wings are shown by black dots. Not only that the mean velocity deficit is nearly zero, but also the velocity fluctuations are small at the optimal locations compared to the wake centerline. The two-point cross-correlation of the cross-stream velocity fluctuations of the flow shown in Figure 2(c) reveals the periodic wake structure, the diffusion and weakening of the wake, and the wavelength. The normalized phase-averaged vorticity and the normalized phase-averaged velocity magnitude at the same phase are shown in Figure 2(d)

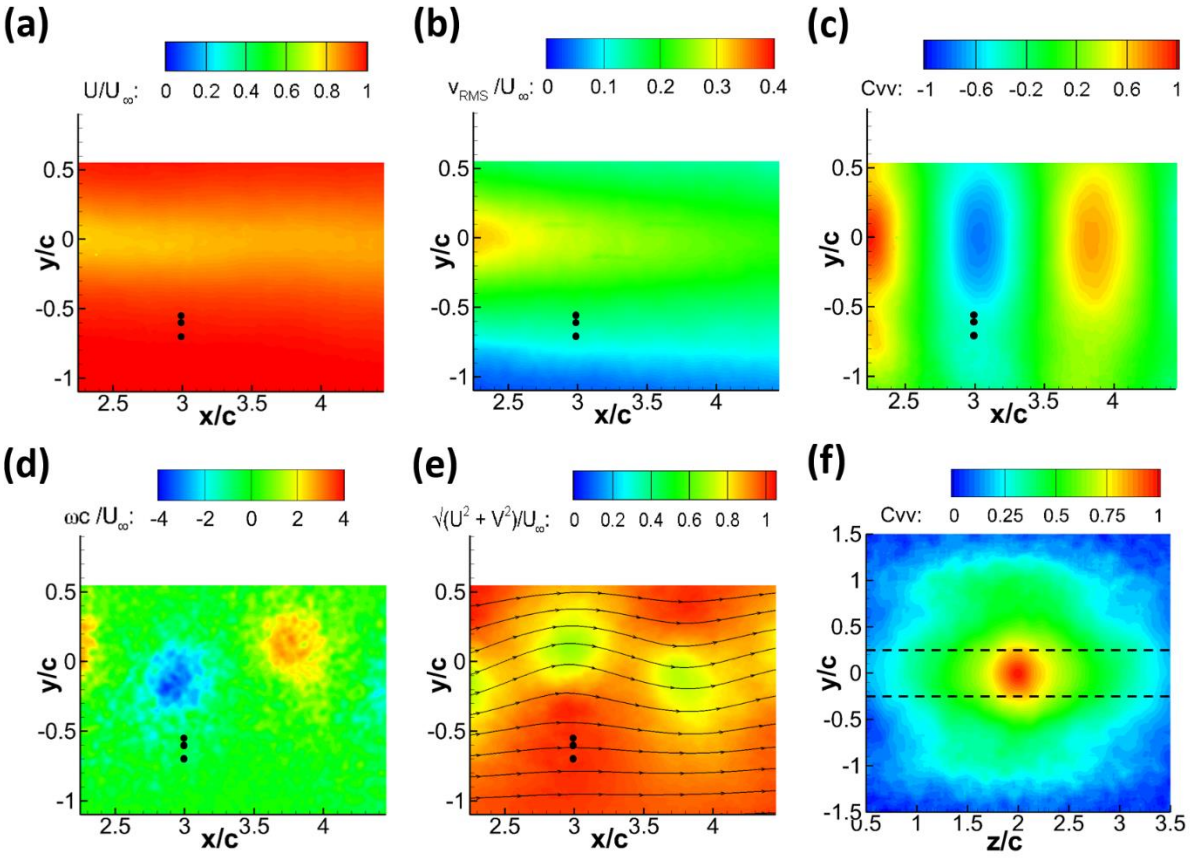

Figure 2: (a) Time-averaged streamwise velocity; (b) rms of cross-stream velocity; (c) cross-correlation of cross-stream velocity component; (d) phase-averaged vorticity; (e) phase-averaged velocity magnitude; (f) cross-correlation contours in cross flow plane downstream of wake generator shown with dashed lines.

and 2(e), respectively. Finally, the two-point cross-correlation of the cross-stream velocity fluctuations in the crossflow plane at x/c = 3 is shown in Figure 2(f). The two-point cross-correlation is defined [32] for the cross-stream velocity component as:

$$C_{vv} = \frac{\overline{v'_A v'_B}}{\sqrt{\overline{v'^2_A}}\sqrt{\overline{v'^2_B}}} \tag{4}$$

where v'_A is the fluctuating cross-stream velocity component at reference point A, and v'_B is the fluctuating cross-stream velocity component at any arbitrary location B in the measured domain. In Figure 2(c) and 2(f), the reference point A was chosen as (x/c = 2.25, y/c = 0) and (y/c = 0, z/c = 2) respectively.

As expected, the wake is symmetrical about y/c = 0 axis in both spanwise plane and streamwise plane. The maximum time-averaged velocity defect of $\Delta U_{max}/U_\infty$ = 0.19 is observed along the wake centreline at x/c = 3 (where the leading edge of the wing is positioned when the wing is placed in the wake). The momentum thickness of the wake, calculated from the velocity defect, at x/c = 3 is θ/c = 0.138. The streamwise wavelength λ_∞ of the wake is determined from the correlation contour to be 1.58c. The circulation of the large-scale vortex in the wake around x/c = 3 is calculated to be $\Gamma U_\infty/c = 0.42$. The cross-correlation integral scale is defined as

$$L/c = \int_{\frac{z}{c}=0.5}^{\frac{z}{c}=3.5} C_{vv}\left(\frac{y}{c}=0, \frac{z}{c}\right) d\left(\frac{z}{c}\right) \tag{5}$$

The cross-correlation integral scale is calculated (from the cross-correlation of the cross-stream velocity) to be L/c = 1.77. The length-scale is roughly three times the thickness of the wake generator, the same order of magnitude as reported for the wake of a circular cylinder [33] and airfoil [34] in the near wake. In our case, the integral length-scale is approximately equal to the wavelength of the vortex street. Since in our case the aspect ratio is varied between sAR = 0.5 and 4, the ratio of the integral length-scale to the wing-span may be important. The Strouhal number of the wake based on the wake generator thickness is 0.26, which corresponds to a Strouhal number based on the chord length of the downstream wing of 0.52 [17].

The variation of the time-averaged lift coefficient with angle of attack for the baseline cases (wings in undisturbed steady freestream) is shown in Figure 3 for unswept wings with AR = 8 (sAR = 4) and with profiles of NACA0012, NACA0006, and flat-plate. The

experimental data are compared with Prandtl's theoretical prediction of infinite and finite wings with elliptical variation of lift per span. In general, the initial slope of all wings is consistent with the lifting line theory. We noticed the *t/c* = 12% flat-plate wing has a lower stall angle compared to other wings. (We note that a thin *t/c* = 1.3% flat-plate at a similar Reynolds number has a larger stall angle as reported by Gutierrez-Castillo *et al*. [35], not presented here). In our case, the lower stall angle might be a result of the thicker profile and the negative camber of our wing. Nevertheless, this has little relevance as the main focus of this article will be on the post-stall regime.

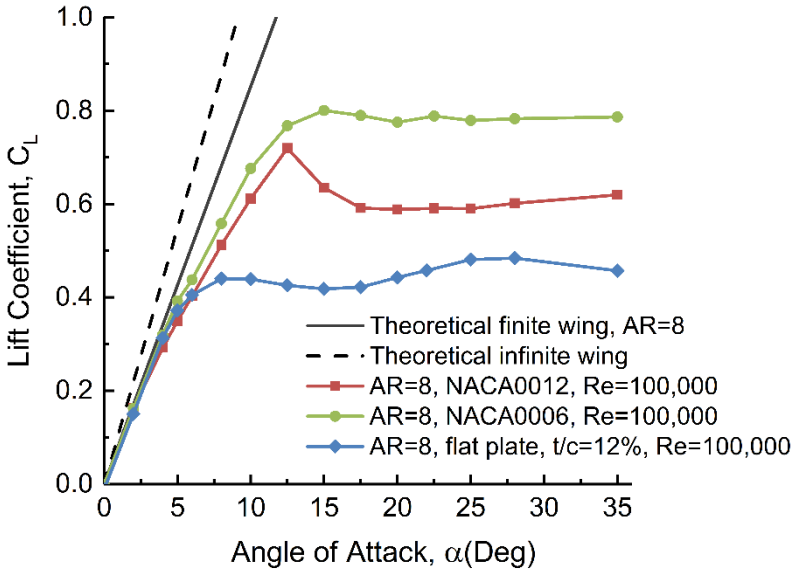

Figure 3: Time-averaged lift coefficient as a function of angle of attack in freestream.

A. Effect of wing aspect ratio

Figure 4 compares the variation of the time-averaged lift coefficient as a function of normalized offset distance y_{LE}/c for varying wing aspect ratio at a post-stall angle of attack of $\alpha = 20^o$. This angle of attack was chosen for comparison since our previous work for *AR* = 8 revealed the maximum lift increase at this angle of attack [17]. For each aspect ratio, the corresponding time-averaged lift coefficient in undisturbed freestream is shown with horizontal dashed lines. For the two lowest aspect ratios, the time-averaged lift can be lower than that in the freestream when the leading-edge is at the wake centerline or slightly above it. However, the time-averaged lift increases compared to the freestream when the leading-edge is located well below the wake centerline and at the edge of the wake shear layer. For aspect ratios larger

than 2, there is lift increase at all locations in the wake. In addition, for all wings, there exists a local maximum in the time-averaged lift. We term this location with maximum lift as the "optimal location".

The optimal location occurred at a similar cross-stream location near the edge of the wake for all tested wings (see also Figure 2(b) for the rms value of the cross-stream velocity fluctuations). Our previous research for AR = 8 [17] suggests that small cross-stream velocity fluctuations at the optimal location always ensure separated flow over the wing with periodic shedding of leading-edge vortices. In contrast, at the wake centerline, the wing undergoes fully attached flow followed by fully stalled flow in the same cycle, with a smaller contribution of the leading-edge vortices. Figure 4 suggests the existence of an optimal location for all wings, although the local maximum for the lowest aspect ratio is less clear. The fact that a similar optimal location is found for all wings indicates that the flow physics is the same for all wings. The maximum lift increase at this angle of attack appears to increase with increasing aspect ratio.

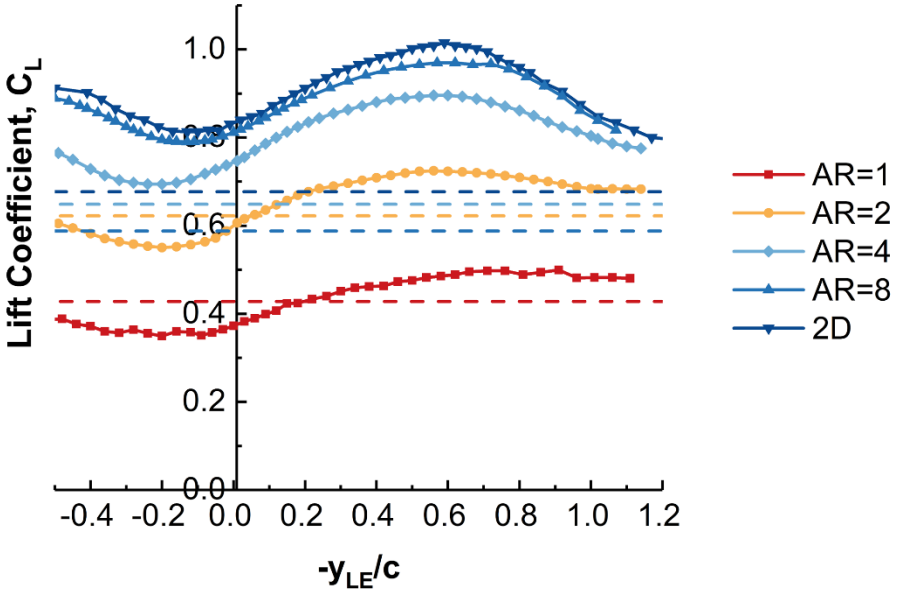

Figure 4: Time-averaged lift coefficient as a function of offset distance for unswept wings with NACA0012 profile at α=20°.

The lift force measurements have been performed at the wake centreline and the individual optimal location for each wing. Figure 5 presents the variation of the time-averaged lift coefficient C_L with angle of attack α for x_{LE}/c =3. When the wing is located in the wake,

the delay of the stall is clear for all wings, except for the lowest aspect ratio. When the wing is located at the wake centreline, for all wings tested, including *AR* = 1, the lift slope at pre-stall

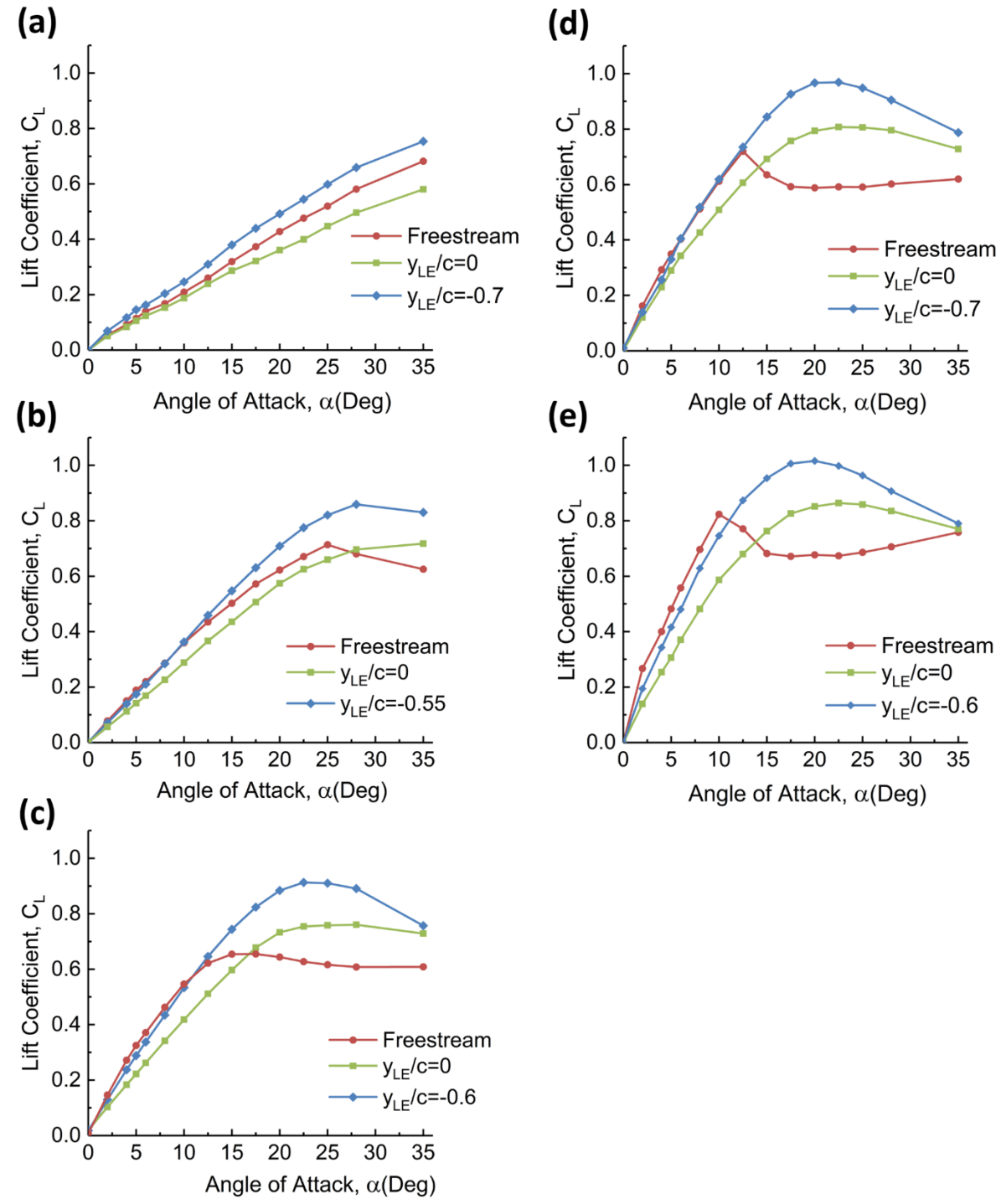

Figure 5: Time-averaged lift coefficient as a function of angle of attack for unswept NACA0012 wings with (a) *AR*=1, (b) *AR*=2, (c) *AR*=4, (d) *AR*=8, (e) *AR*=∞.

angles of attack decreases, while the maximum lift coefficient may differ slightly. In contrast, for optimal locations, the lift slope at pre-stall angles of attack remains nearly the same as in

freestream, however remarkable increases in the maximum lift coefficient are observed at post-stall angles of attack. The maximum lift coefficient of C_L = 1.01 is found for the 2D airfoil. Figure 6 compares the maximum lift coefficient in the wake and in the freestream for each wing. Both lift coefficients increase with increasing aspect ratio, consistent with the expected effect of the wing-tip and downwash of the tip vortices.

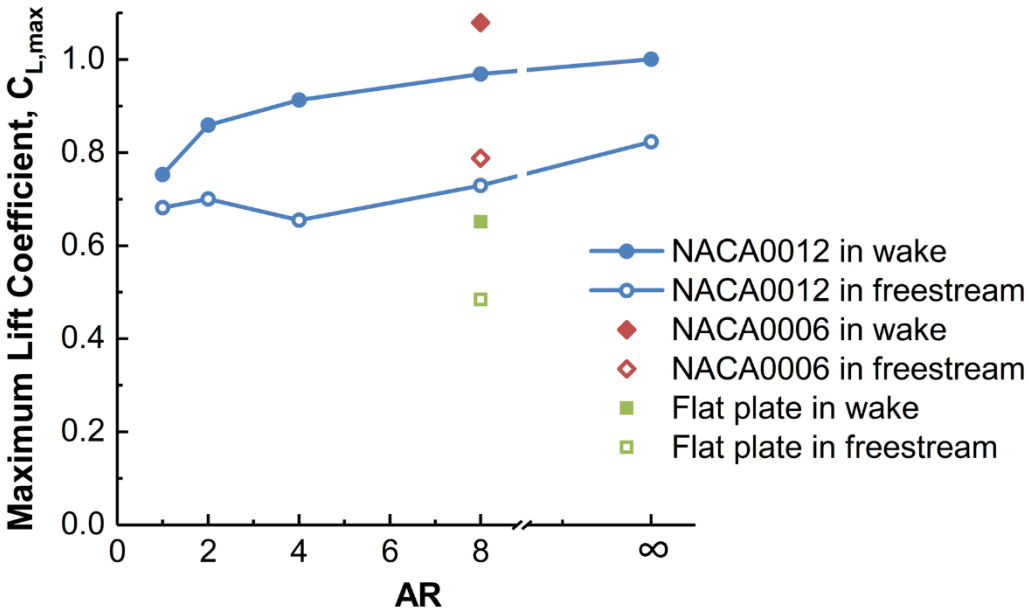

Figure 6: Maximum lift coefficient as a function of aspect ratio of wings in the wake compared with that in freestream.

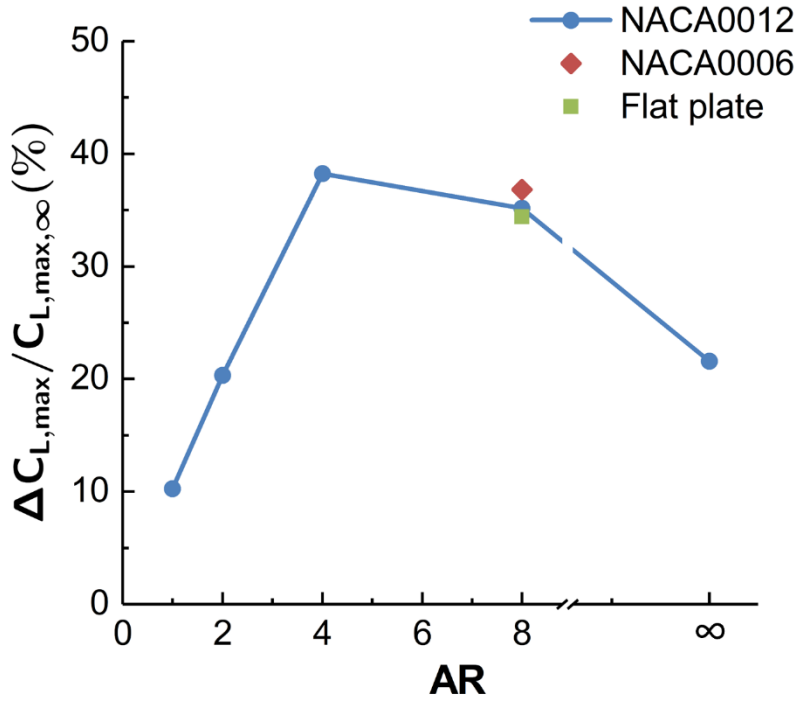

Figure 7: Percentage increase of maximum lift coefficient as a function of aspect ratio.

However, the maximum lift enhancement is not necessarily found for the 2D airfoil. The maximum increase in the lift coefficient is seen for AR = 4 and 8 wings as approximately $\Delta C_L \approx 0.25$. Due to the smaller maximum lift coefficient in freestream, there is a higher percentage increase (38%) for the AR = 4 wing. Figure 7 shows the percentage increase of the maximum lift coefficient as a function of aspect ratio. For aspect ratios larger than AR = 4, there is a gradual decrease in the percentage lift enhancement. This may be because of the finite spanwise length scale (L/c = 1.77) of the incident wake as discussed previously. For the aspect ratio AR = 4 (sAR = 2), the spanwise length scale of the incident wake is close to the wing-span ($2c$) on which the unsteady lift acts. This means that the unsteady local lift will be close to being fully correlated over the whole wing for this aspect ratio. In contrast, for larger aspect ratios, local lift over the whole wing will not be fully correlated and may even cancel the contributions in other parts of the wing when averaged over time. On the other hand, this reasoning leads to the expectation that smaller aspect ratios will be equally effective as the local lift will be fully correlated over the whole wing. Figure 6 shows the opposite. This is due to the varying strength of the leading-edge vortices, which are the main source of the enhanced lift in the wakes. To clarify we have carried out detailed measurements for all wings at the same angle of attack of $\alpha = 20^o$.

Figure 8 presents the time-averaged velocity magnitude contours at halfway across the semi-span of the unswept wings at $\alpha = 20^o$ in freestream and when the wing is placed at the optimal cross-stream location. For all wings, in freestream, there is a large recirculation region in the time-averaged flow, indicating the completely separated flow without reattachment. Due to the downwash and reduced effective angle of attack for smaller AR wings, the separated region appears slightly smaller in size with decreasing AR of the wing. This can be noticed by comparing AR = 2 and ∞. At the optimal location of the wing in the wake, a large recirculation region and separation bubble (in the time-averaged sense) is visible at high aspect ratios. As the aspect ratio is decreased, the time-averaged separation bubble decreases in size and eventually disappears for the AR = 2 wing. This corresponds to a decrease in the curvature of the streamlines over the wing in a time-averaged sense, resulting in a smaller lift coefficient for wings with small AR. The time-averaged flows shown in Figure 8 suggest that substantial drag reduction is expected to accompany the lift enhancement.

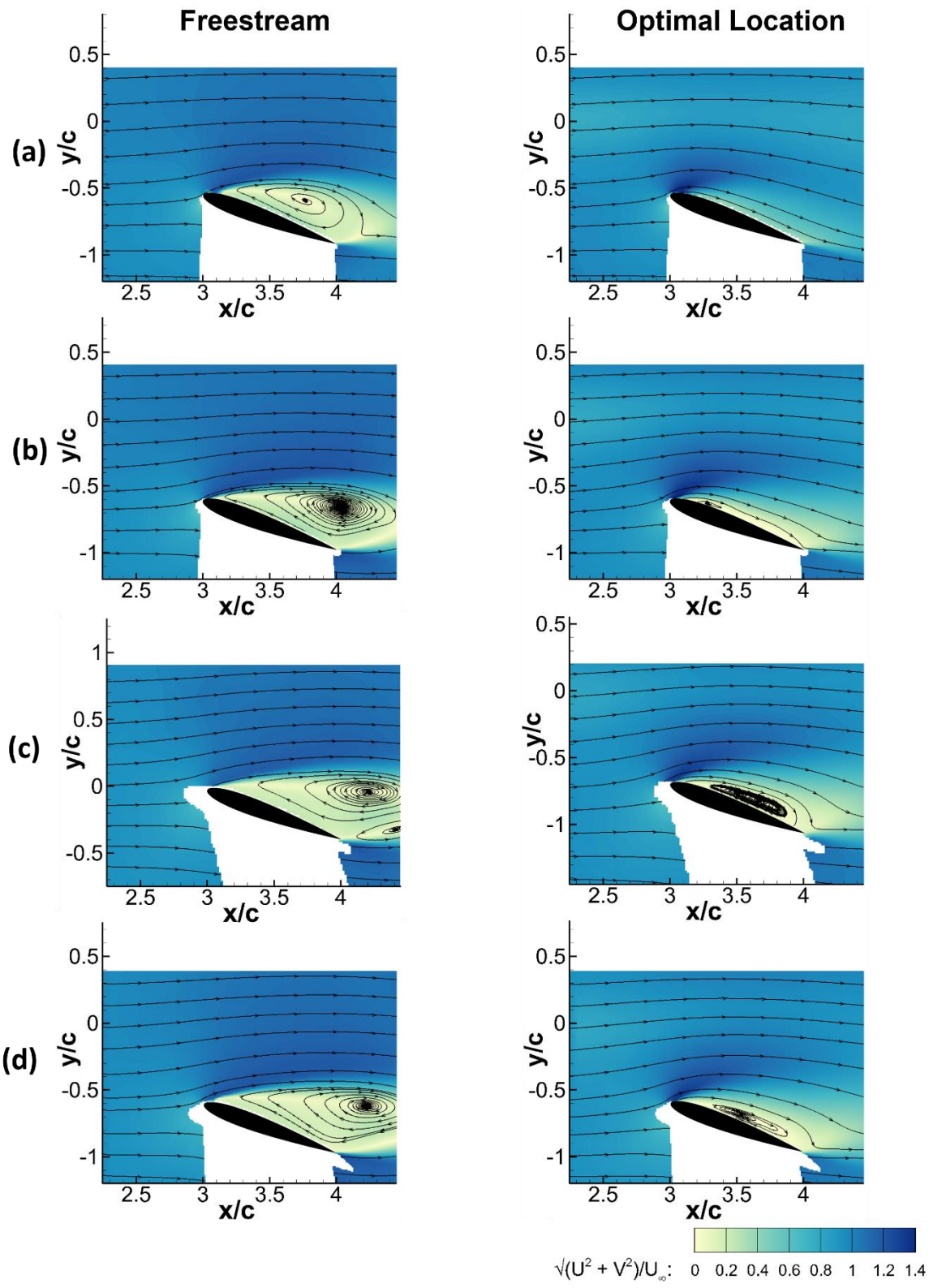

Figure 8: Time-averaged velocity magnitude contours for unswept wings at $\alpha=20^{o}$, measured at $z/c=2$, for (a) $AR=2$, (b) $AR=4$, (c) $AR=8$, (d) $AR=\infty$, in freestream and optimal location in the wake.

For $\alpha = 20°$, Figures 9 and 10 compare the phase-averaged vorticity contours at halfway across the semi-span for the 2D airfoil and $AR = 2$ wing, respectively, at the optimal locations of the wings. For the 2D airfoil (Figure 9), the upper surface shear layer starts to roll-up to coherent LEV structures as the wake vortex with positive sign approaches the leading edge ($t/T = 0.25$, but the incident vortex is not visible yet). The positive incident vortex starts entering the field of view around $t/T = 0.5$ and becomes fully visible afterwards. The growth of the LEV is visible, and at a later stage the LEV sheds and convects downstream. At the latest stages $t/T = 0.875$, 0, 0.125, there is a weakening of the vorticity field rapidly as the vortex becomes presumably more three-dimensional. Nevertheless, a large separation bubble and a strong LEV is seen throughout the cycle. Because of their large size, at some instants ($t/T = 0$ and 0.125) it is somewhat difficult to define a boundary to separate two successive LEVs.

In contrast, the LEV boundary is well defined, and the separation bubble is much smaller on the $AR = 2$ wing (see Figure 10). The birth of the LEV is first noticed at $t/T = 0.125$. Its growth is visible until t/T=0.5, followed by shedding afterwards. The LEV is much smaller, both in size and strength, than its 2D airfoil counterpart. At $t/T = 0.625$, as the positive incident vortex approaches the mid-chord, the shedding process starts. The shed LEV moves away from the wing surface and dissipates into the wake, while the flow near the leading-edge region becomes almost attached at t/T = 0.875 and 0. Effectively, the small aspect ratio wing behaves as if it is in "light stall" with some excursion to the separated flow regime, whereas the 2D airfoil undergoes "deep stall" and remains in the separated flow regime all the time. This major difference can be attributed to the fact that the small aspect ratio wing operates at a smaller effective angle of attack due to the downwash of the tip vortex. Although the mean (geometric) angle of attack is the same ($\alpha = 20°$) in both cases, the effective angle of attack is somewhat smaller for the low aspect ratio wing. This results in light stall for the low aspect ratio wing in the same wake. In summary, the aspect ratio of the wing determines the degree of "stall", which was described in detail by Ekaterinaris & Platzer [20] for pitching and plunging wings. We note that wake vortices induce the LEVs in our case as opposed to a wing motion.

Noting the similarities of the LEVs in our experiments with the dynamic stall vortices, one would expect that the size and the circulation of the LEVs should be directly correlated with the time-averaged lift enhancement. Using the selected boundaries shown with dashed lines in Figures 9 and 10, the circulation of the LEVs is calculated and presented in Figure 11. It is seen that the maximum circulation is similar for the $AR = 8$ wing and the 2D airfoil. In contrast, for smaller aspect ratio wings, the maximum circulation decreases with decreasing

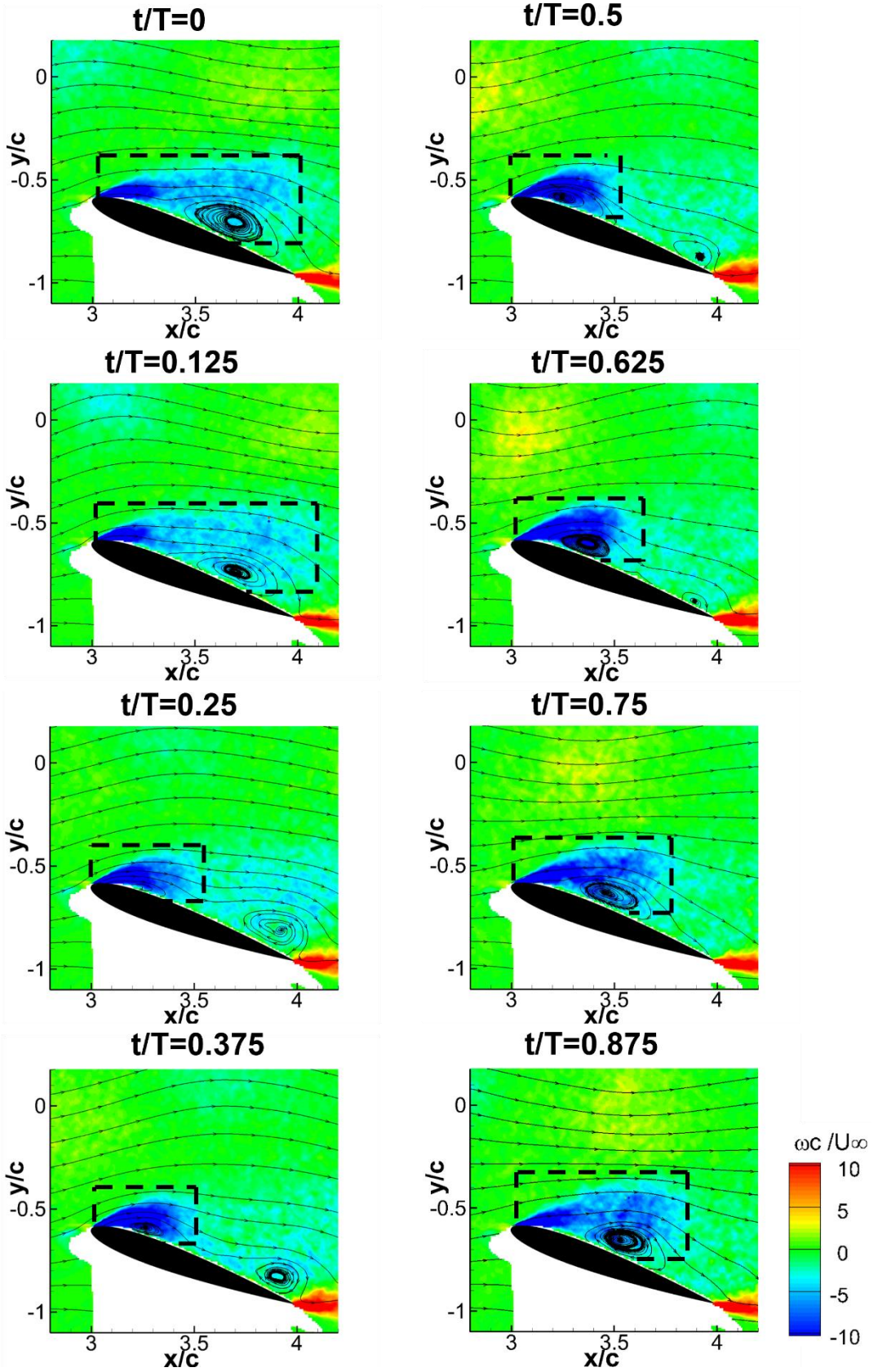

Figure 9: Phase-averaged vorticity superimposed with streamlines for unswept airfoil, $AR = \infty$, at $\alpha=20^{o}$, for the optimal location of the wing in the wake.

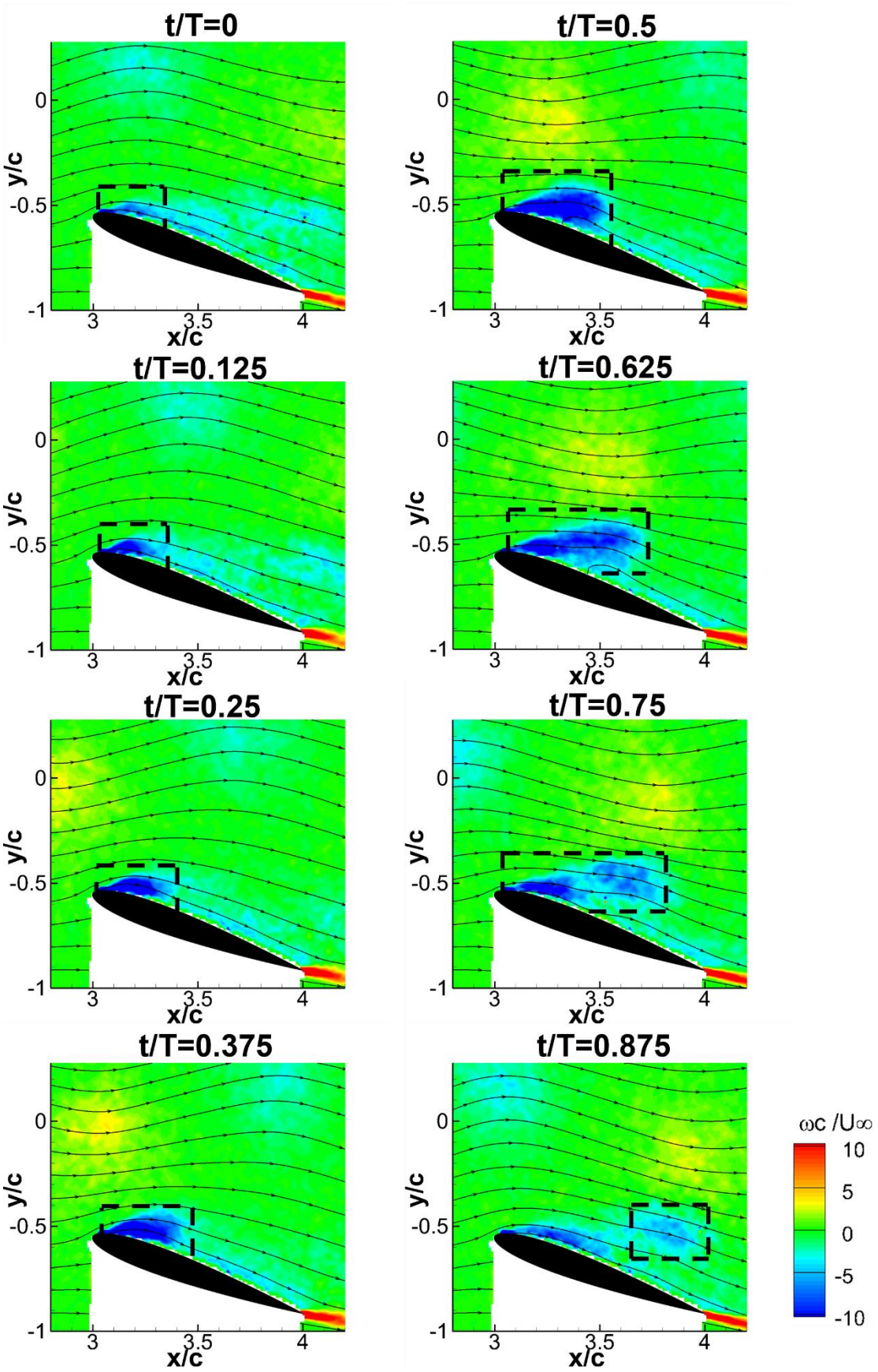

Figure 10: Phase-averaged vorticity superimposed with streamlines for unswept wing, *AR* = 2, at α=20^{o} for the optimal location of the wing in the wake.

aspect ratio. In Figure 11, the phase-averaged vorticity fields with streamlines at the instant of the maximum circulation are shown in the right column. With increasing aspect ratio, we observe highly curved streamlines, large separation bubbles, and the flow reattachment near the trailing-edge. The highly curved streamlines and reattachment disappear with decreasing aspect ratio, as the wings see smaller effective angles of attack due to the downwash of the tip vortices.

Figure 12 summarizes the maximum circulation of the leading-edge vortices for each wing. The maximum circulation is found at $AR = 8$ and is slightly less for the 2D airfoil. A similar observation in the context of dynamic stall is reported by Phillips *et al*. [36] for flapping wings. They showed that the LEV circulation (a major factor for lift enhancement during dynamics stall) peaks at AR=6 during dynamic stall. For low aspect ratios, the increase of the maximum circulation with increasing aspect ratio is similar to the increase in the lift enhancement shown in Figure 7.

B. Effect of wing sweep angle

Figure 13(a) presents the time-averaged lift coefficient as a function of the normalized offset distance y_{LE}/c for varying wing sweep angle at a post-stall angle of attack of $\alpha = 20^{o}$. The horizontal dashed lines correspond to the time-averaged lift coefficients measured in freestream. When submerged in the wake, the mean lift decreases with increasing sweep angle, with a slight shift in the optimum location away from the wake centerline. Figure 13(b) shows the percentage increase of maximum time-averaged lift coefficient compared to the freestream at $\alpha = 20^{o}$ as a function of sweep angle. The percentage lift enhancement shows strong dependence with the sweep angle. With a 40^{o} sweep, the lift enhancement drops to less than one-third of that of the reference straight wing. These results are in agreement with the observations of the gust encounters with swept wings [25,26]. For zero sweep angle, the wake disturbances will be acting on the whole span of the wing simultaneously. With increasing sweep angle, the effective span of the wing that will interact with the wake at a given instant will decrease as $\cos(\Lambda)$, resulting in decreased two-dimensionality. This is the natural consequence of the relative magnitude of the wavelength of the wake disturbances ($\lambda_\infty/c \approx 1.6$). If the wavelength were very large, the decrease in the two-dimensionality would be smaller.

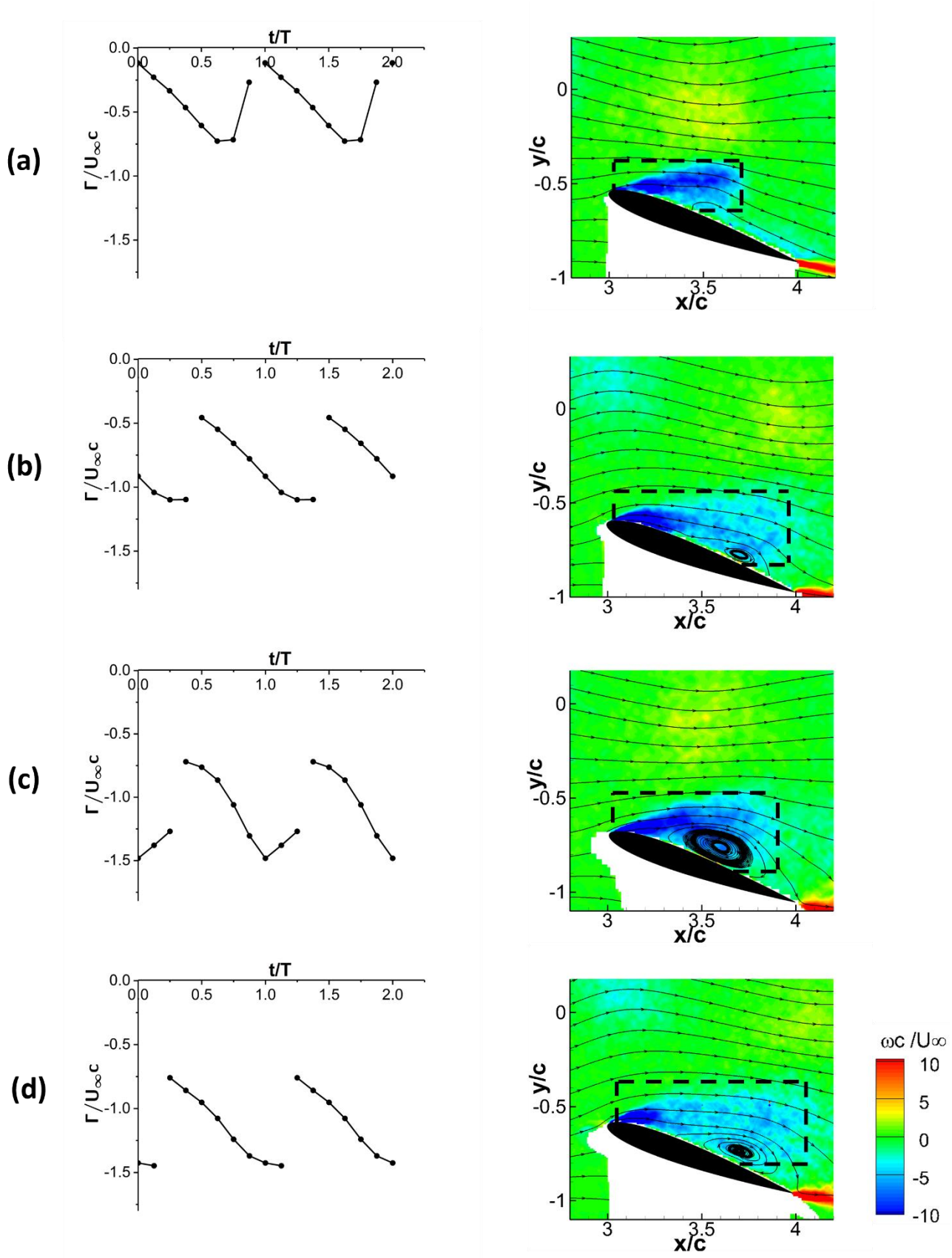

Figure 11: Time history of normalized circulation of LEV (left column) and phase-averaged vorticity contours at the instance of the maximum circulation (right column) for unswept wings at $\alpha=20^{o}$ for (a) *AR*=2, (b) *AR*=4, (c) *AR*=8, (d) *AR*=∞ for the optimal location of the wing.

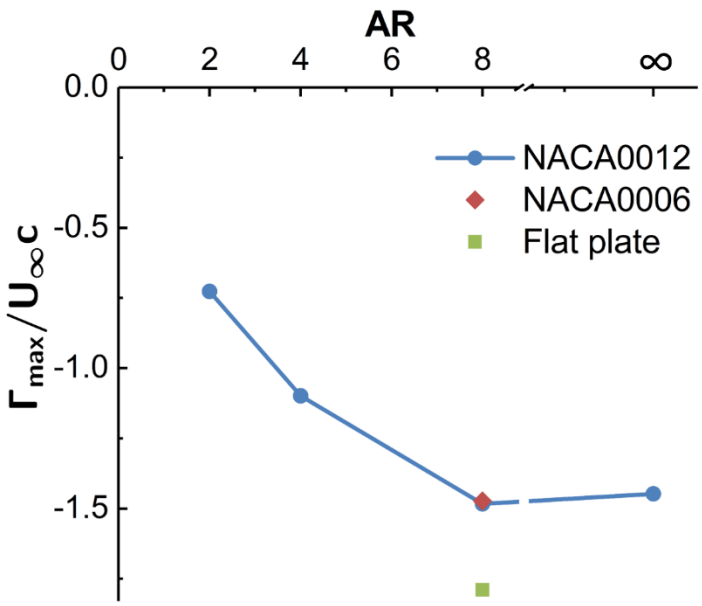

Figure 12: Maximum LEV circulation as a function of aspect ratio.

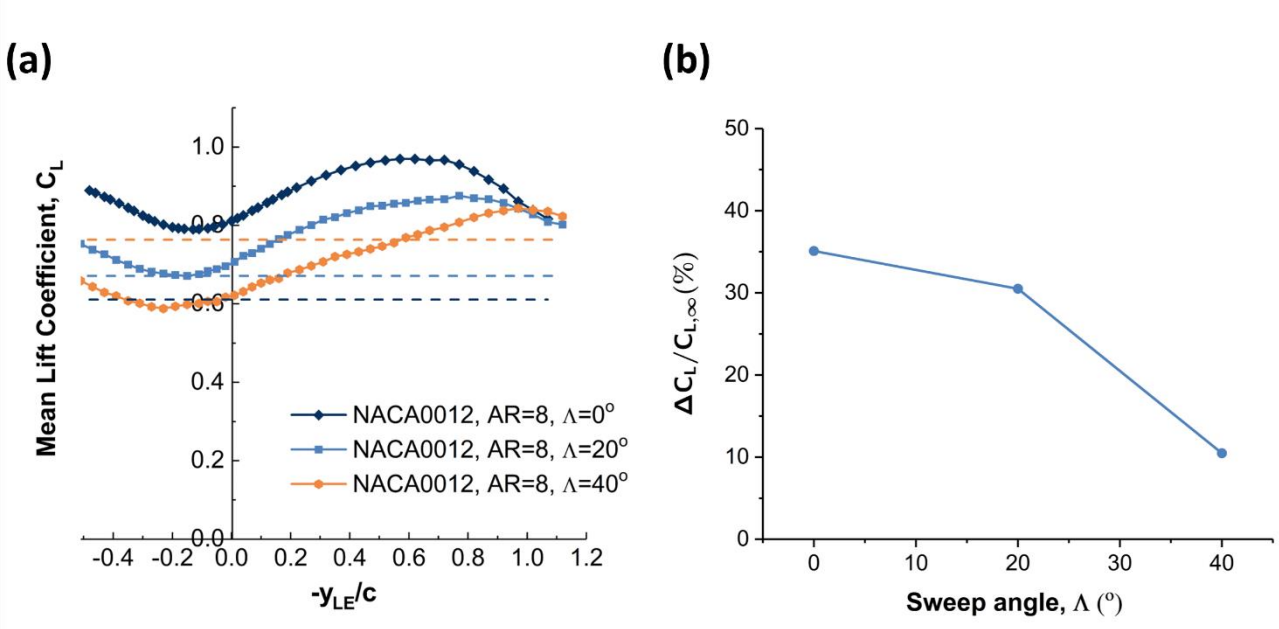

Figure 13: (a) Time-averaged lift coefficient as a function of offset distance; (b) maximum percentage increase of lift coefficient compared to that in freestream as a function of sweep angle; $\alpha=20^o$.

C. Effect of leading-edge shape

Figure 14 compares the time-averaged lift coefficient as a function of normalized offset distance y_{LE}/c for three different wing profiles at a post-stall angle of attack of $\alpha = 20^{o}$. The horizontal dashed lines correspond to the time-averaged lift coefficients measured in freestream. For NACA0006 and flat plate wings, the existence of the optimal location at a similar non-zero cross-stream location is similar to the previous observations of the NACA0012 profiled wing. For the NACA0012 and NACA0006 profiled wings, negligible difference is seen at positive cross-stream offset distances. Whereas, at negative y_{LE}/c, the two curves deviate, with the NACA0006 generating slightly higher lift at all negative cross-stream locations compared to the NACA0012 profiled wing. However, despite the slightly less lift, the NACA0012 profiled wing boosts a much higher percentage lift increase than the NACA0006 counterpart, due to the lower lift generated in freestream. As for the flat plate wing, due to the early stall characteristics, it generates the least lift among the three wings, both in freestream and in the wake.

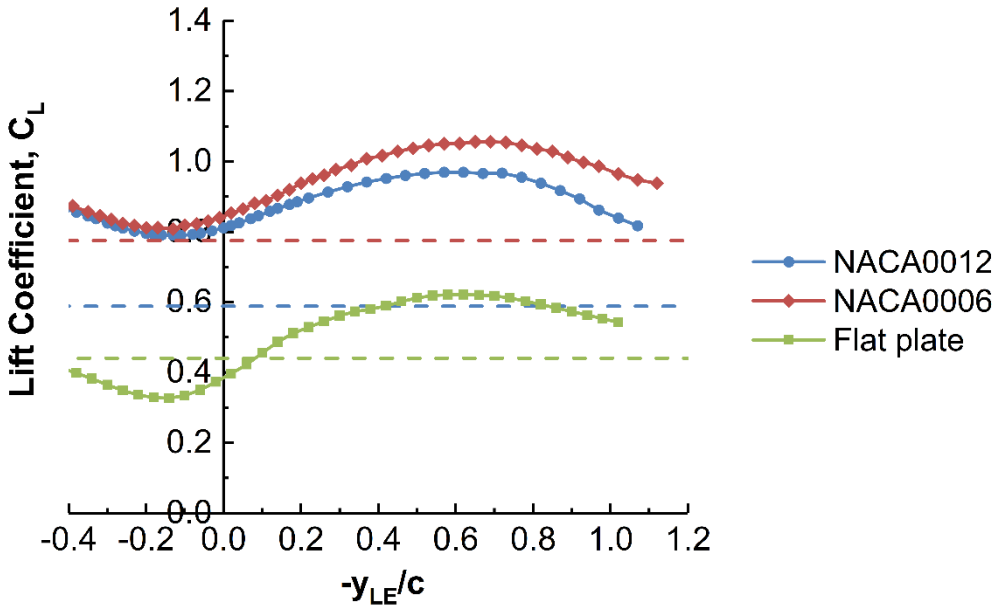

Figure 14: Time-averaged lift coefficient as a function of offset distance for various airfoil profiles, *AR*=8 and α=20^{o}.

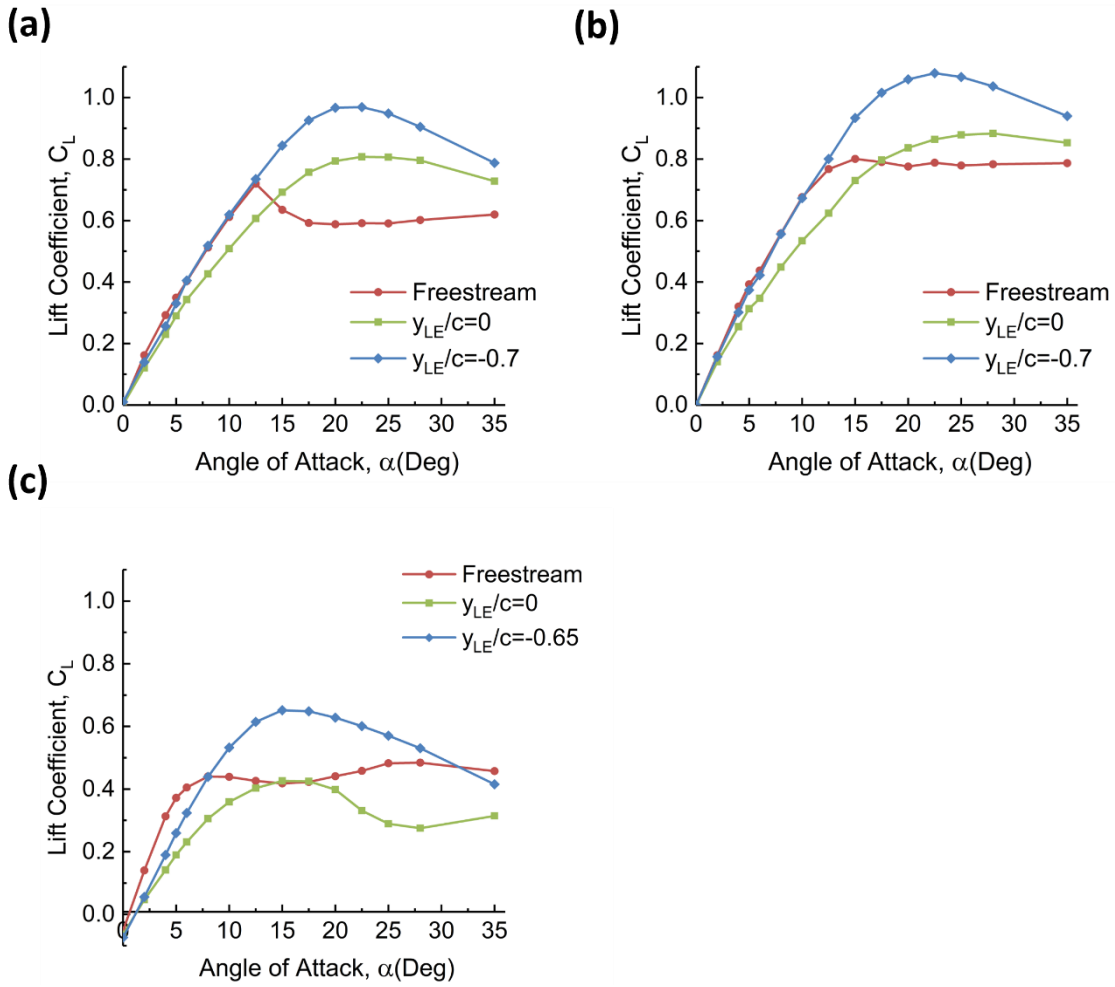

Figure 15: Time-averaged lift coefficient as a function of angle of attack for (a) NACA0012; (b) NACA0006; (c) flat plate; *AR*=8.

The variation of the time-averaged lift coefficient C_L with angle of attack α for the three different wings placed at the wake centreline, optimal offset location and in the freestream are presented in Figure 15. When the wing is placed in the wake, for both cross-stream locations, the delay of stall is apparent for all three wings. At the wake centerline, the reduced lift curve slope with little change in the maximum lift is similar to the previous observations. In contrast, at the optimal offset locations, the lift curve remains nearly the same as in freestream at pre-stall angles of attack for NACA0006 but a slightly smaller slope than in freestream is observed for the flat plate wing. The maximum lift exhibits a remarkable increase at post-stall angles of attack for both NACA0006 and flat plate wings. A maximum lift coefficient of C_L =1.08 is observed for the NACA0006 wing, which is 11% higher than the NACA0012 wing and a 35% enhancement compared to the maximum lift coefficient generated in freestream. The maximum lift is measured at α = 20° for NACA0012, α = 22.5° for NACA0006 and α = 15° for the flat

plate wing, all of which are 7.5 degrees higher than the stall angle of each individual wing in freestream. Therefore, we conclude that the delay in the stall angle is not affected by the wing profile.

Returning to Figures 6 and 7, the effect of wing profile can be seen at AR = 8. The NACA0006 wing generated the highest lift both in the wake and in freestream while the flat plate wing produced the least lift. However, the percentage increase of the maximum lift coefficient calculated from $(C_{L,max} - C_{L,max,\infty})/\ C_{L,max,\infty}$ is similar for all three wing profiles. In order to understand the differences and similarities, we compare the variation of circulation and phase-averaged flow for all three wings.

We present the variations of the circulation of the LEVs in Figure 16 in the left column. It is seen that the maximum LEV circulation is similar for NACA0012 and NACA0006, but in both cases it is lower than that of the flat plate, although the latter has the lowest time-averaged lift. The stronger LEVs for the flat-plate wing in the wake, compared to the wings with rounded leading-edge, are consistent with observations for plunging airfoils and wings [27,28]. The phase-averaged vorticity fields with streamlines at the instant of the maximum circulation are also shown in the right column of Figure 16. It is seen that the LEV on the flat plate wing is further away from the wing surface compared to the wings with rounded leading-edge. This suggests that the LEVs on the flat-plate generate less suction, thus lower lift is expected. As for the NACA0006 wing, the growth of the circulation is more gradual, and the circulation remains close to the maximum value for a longer period of time compared to the NACA0012 wing, thus a higher mean value over the same period.

The state of the flow (separated versus attached) is monitored by means of the local flow angle, $tan^{-1}(\langle v \rangle / \langle u \rangle)$ at the location C (see the insert in Figure 17). This particular location was chosen as it is sufficiently away from the surface to be able to obtain reliable velocity measurements, yet not too far away to be able to monitor the local flow near the leading-edge. For each wing, the corresponding flow angle at location C in steady freestream is also shown with horizontal dashed lines in Figure 17 for $\alpha = 20^o$. When the wings are located at the optimal location, the flow angle at C has small amplitude oscillations around a mean which is slightly higher than that in the steady freestream. The time-dependent local flow angle occasionally drops below that in the freestream, but the flow always remains separated throughout the entire cycle. (Completely attached flow at the location C would imply a local flow angle close to zero or a negative value for $\alpha = 20^o$). Our previous work [17] suggests that

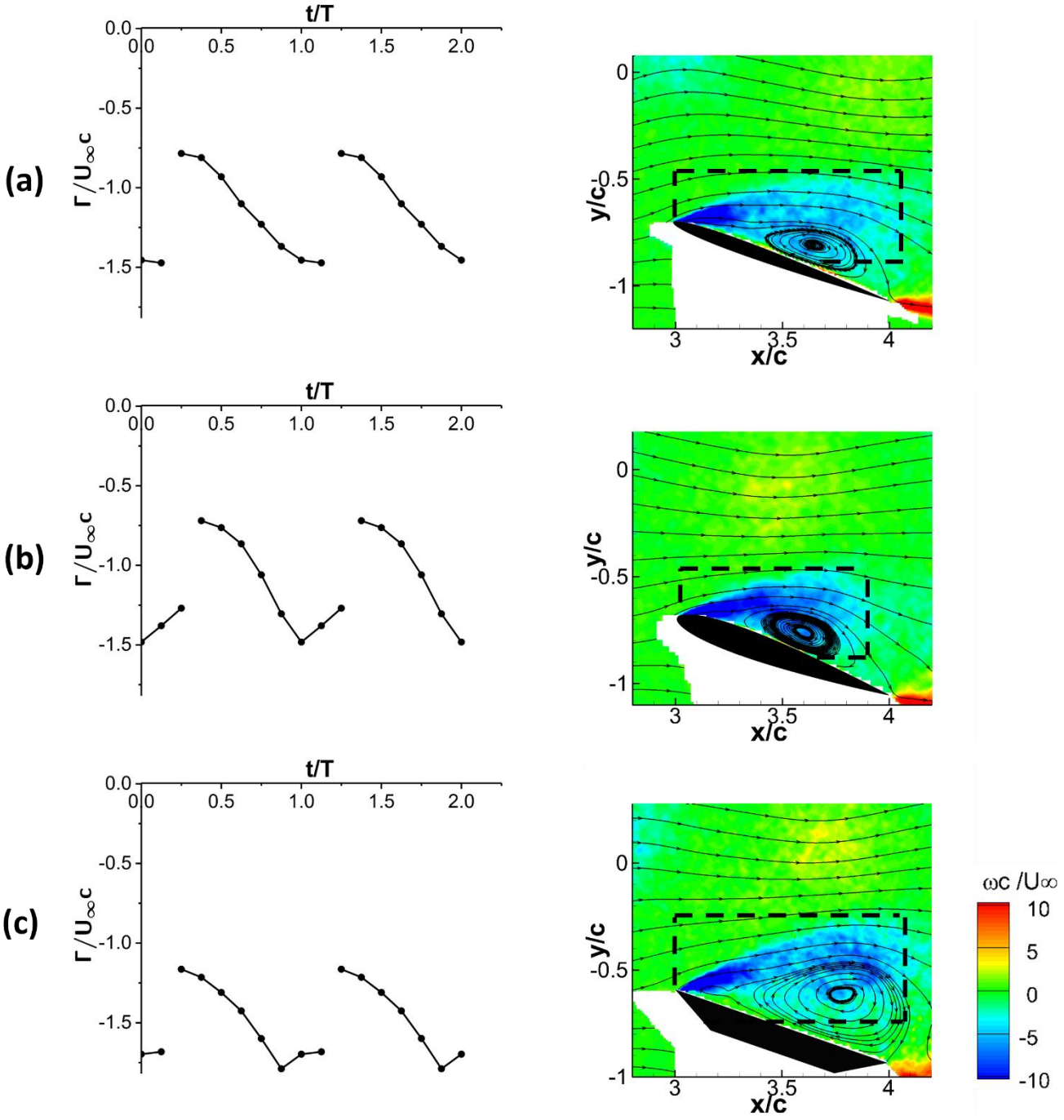

Figure 16: Time history of normalized LEV circulation (left column) and the phase-averaged vorticity contours at the instance with maximum LEV circulation (right column) for (a) NACA0006; (b) NACA0012; (c) flat plate profiles; *AR*=8, α=20^o, and the optimal location in the wake.

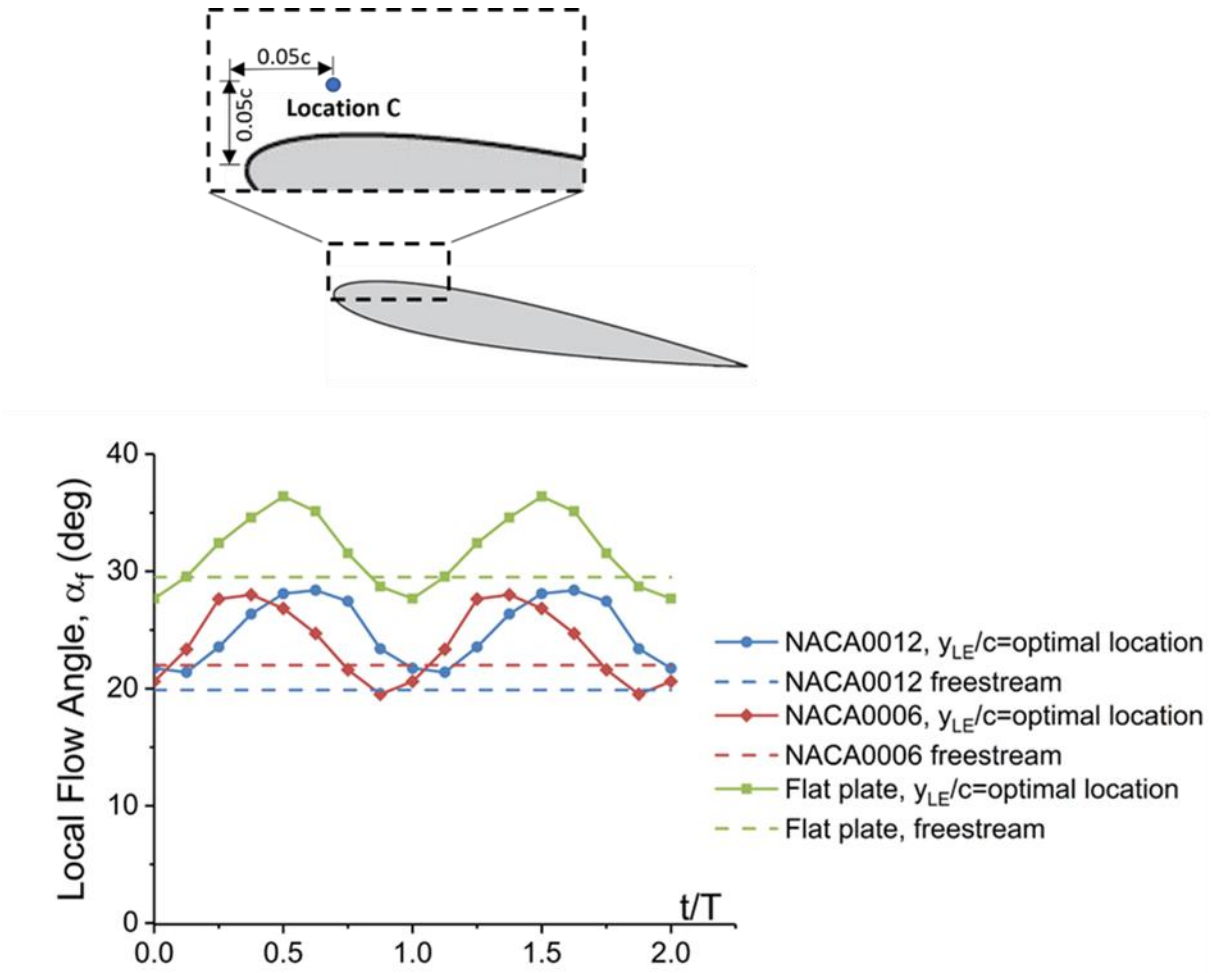

Figure 17: Local flow angle measured at 0.05*c* above and downstream of the leading-edge for wings with different profiles at the optimal location in the wake, *AR*=8 and α=20°.

the small flow angle oscillations around the value in steady freestream is effective to cause periodic formation and shedding of strong LEVs, which are directly associated with the lift enhancement.

IV. Conclusions

The effects of aspect ratio, sweep angle, and the leading-edge geometry for wings placed in a turbulent wake were investigated in wind tunnel experiments at a chord Reynolds number of $Re_c = 10^5$. The post-stall lift enhancement due to the leading-edge vortex formation was studied as the wing geometry influenced the strength of the leading-edge vortices, the ratio of the spanwise length scale of the incident vortex to the wing-span, and the degree of the two-dimensionality of the wake-wing interaction. For all wings of varying aspect ratio, cross-

sectional profile and sweep angle there exist optimal locations with maximum time-averaged lift at a post-stall angle of attack. These optimal locations are always located at the edge of the wake, similar to our previous observations.

When the wing is located at the optimal location, there are two factors that affect the lift enhancement: (i) the ratio of the spanwise length scale of the incident wake to the wing-span, which is inversely proportional to the aspect ratio for a given wake; (ii) the strength (circulation) of the leading-edge vortices that shed from the wing as a result of the interaction. These two factors are expected to affect the time-averaged lift increase in opposite directions. Increasing ratio of the spanwise length scale of the incident wake to the wing-span (decreasing aspect ratio) will result in more synchronized flow over the wing-span, hence should be beneficial for the time-averaged lift. In contrast, the strength of the vortices and the time-averaged lift should increase with increasing aspect ratio as the effective angle of attack (geometric angle of attack minus induced angle of attack due to the tip vortices) increases. Our measurements reveal that the maximum lift coefficient increases with increasing aspect ratio. We observe that the circulation of the leading-edge vortices also increases with increasing aspect ratio initially, but there is little change for $AR \geq 8$. Relative to the wing in freestream, the maximum lift enhancement becomes maximum at an aspect ratio of $AR = 4$. For the aspect ratio of $AR = 4$ (tested as $sAR = 2$), the spanwise length scale of the incident wake is closest to the effective wing-span on which the unsteady lift acts. For larger aspect ratios, the unsteady local lift is not fully correlated over the entire wing-span. For smaller aspect ratios, the spanwise length scale is larger than the effective wing-span, but the circulation decreases rapidly with decreasing aspect ratio. Hence, the competition between the ratio of the wing-span to the spanwise length scale of the incident wake and the strength of the leading-edge vortices determine the optimal aspect ratio.

The effect of the wing sweep angle has been found to be significant. This was expected as the wavelength of the incident vortices in the wake is on the same order of magnitude as the chord length. As the sweep angle increases, the effective spanwise section of the wing that will be interacting with the wake vortices decreases, resulting in decreased two-dimensionality. When submerged in the wake, the mean lift decreases with increasing sweep angle. For the highest sweep angle of 40 deg, the lift enhancement drops to nearly one-third of the unswept wing.

The leading-edge shape affects the maximum lift coefficient because the strength of the leading-edge vortices and their distance from the wing surface depend on the leading-edge

geometry. The thinner profile NACA0006 produced higher lift coefficient than the NACA0012 wing, however the flat-plate wing with sharp leading-edge generated the lowest lift in the wake, despite of producing the strongest leading-edge vortices. This was explained by the observation that the vortices shed from the flat-plate wing remained furthest from the wing surface. The percentage increase of the maximum lift coefficient is similar for all three profiles. Also, the magnitude of the delay of the stall angle at the optimal location is similar for all three shapes. At post-stall angles of attack, separated flow and LEVs are likely to be less sensitive to Reynolds number. We believe that the main features of stall delay and increased maximum lift can also be observed at much higher Reynolds numbers.

Acknowledgments

The authors would like to acknowledge the funding from the University of Bath PhD studentship for the first author.

References

[1] Scharpf, D. F., and Mueller, T. J., "Experimental study of a low Reynolds number tandem airfoil configuration," *Journal of Aircraft*, Vol. 29, No. 2, 1992, pp. 231-236. https://doi.org/10.2514/3.46149

[2] Yuan, G., Xia, J., and Duan, H., "A continuous modeling method via improved pigeon-inspired optimization for wake vortices in UAVs close formation flight," *Aerospace Science and Technology*, Vol. 120, 2022, p. 107259. https://doi.org/10.1016/j.ast.2021.107259.

[3] Shi, Y., Li, G., Su, D., and Xu, G., "Numerical investigation on the ship/multi-helicopter dynamic interface," *Aerospace Science and Technology*, Vol. 106, 2020, p. 106175. https://doi.org/10.1016/j.ast.2020.106175

[4] Hodson, H. P., and Howell, R. J., "Blade-row interactions, transition, and high-lift aerofoils in low-pressure turbines," *Annual Review of Fluid Mechanics*, Vol. 37, 2005, pp. 71-98. https://doi.org/10.1146/annurev.fluid.37.061903.175511

[5] Bie, D., and Li, D., "Numerical analysis of the wing–wake interaction of tandem flapping wings in forward flight," *Aerospace Science and Technology*, Vol. 121, 2022, p. 107389. https://doi.org/10.1016/j.ast.2022.107389

[6] Rockwell, D., "Vortex-body interactions," *Annual Review of Fluid Mechanics*, Vol. 30, No. 1, 1998, pp. 199-229. https://doi.org/10.1146/annurev.fluid.30.1.199

[7] Barnes, C. J., and Visbal, M. R., "Angle of attack and core size effects on transitional vortical-gust–airfoil interactions," *AIAA Journal*, Vol. 58, No. 7, 2020, pp. 2881-2898. https://doi.org/10.2514/1.J058654

[8] Gursul, I., and Rockwell, D., "Vortex street impinging upon an elliptical leading edge," *Journal of Fluid Mechanics*, Vol. 211, 1990, pp. 211-242. https://doi.org/10.1017/S0022112090001550

[9] Peng, D., and Gregory, J. W., "Asymmetric distributions in pressure/load fluctuation levels during blade-vortex interactions," *Journal of Fluids and Structures*, Vol. 68, 2017, pp. 58-71. https://doi.org/10.1016/j.jfluidstructs.2016.10.008

[10] Durgesh, V., Padilla, R., Garcia, E. N., and Johari, H., "Impact of Coherent Structures on Aerodynamics Performance at Low Reynolds Numbers," *AIAA Science and Technology Forum and Exposition (SciTech 2019)*, San Diego, California, United States, 7-11 January 2019. AIAA 2019-0847.
https://doi.org/10.2514/6.2019-0847
[11] Lefebvre, J. N., and Jones, A. R., "Experimental Investigation of Airfoil Performance in the Wake of a Circular Cylinder," *AIAA Journal*, Vol. 57, No. 7, 2019, pp. 2808-2818.
https://doi.org/10.2514/1.J057468
[12] Zhang, Z., Wang, Z., and Gursul, I., "Lift Enhancement of a Stationary Wing in a Wake," *AIAA Journal*, Vol. 58, No. 11, 2020, pp. 4613-4619.
https://doi.org/10.2514/1.J059872
[13] Ravi, S., Watkins, S., Watmuff, J., Massey, K., Peterson, P., and Marino, M., "Influence of Large-Scale Freestream Turbulence on the Performance of a Thin Airfoil," *AIAA Journal*, Vol. 50, No. 11, 2012, pp. 2448-2459.
https://doi.org/10.2514/1.J051640
[14] Hoffmann, J. A., "Effects of freestream turbulence on the performance characteristics of an airfoil," *AIAA Journal*, Vol. 29, No. 9, 1991, pp. 1353-1354.
https://doi.org/10.2514/3.10745
[15] Kay, N. J., Richards, P. J., and Sharma, R. N., "Influence of Turbulence on Cambered and Symmetrical Airfoils at Low Reynolds Numbers," *AIAA Journal*, Vol. 58, No. 5, 2020, pp. 1913-1925.
https://doi.org/10.2514/1.J058822
[16] Li, L., and Hearst, R. J., "The influence of freestream turbulence on the temporal pressure distribution and lift of an airfoil," *Journal of Wind Engineering and Industrial Aerodynamics*, Vol. 209, 2021, p. 104456.
https://doi.org/10.1016/j.jweia.2020.104456
[17] Zhang, Z., Wang, Z., and Gursul, I., "Aerodynamics of a wing in turbulent bluff body wakes," *Journal of Fluid Mechanics*, Vol. 937, 2022, pp. A37 1-26
https://doi.org/10.1017/jfm.2022.132
[18] Knight, M., and Wenzinger, C. J., "Wind-tunnel tests on a series of wing models through a large angle of attack range. Part I: force tests," *Annual Report-National Advisory Committee for Aeronautics*, Vol. 15, 1929, pp. 255-303.
https://doi.org/10.1016/s0016-0032(30)91021-6
[19] Jones, R., Cleaver, D. J., and Gursul, I., "Aerodynamics of biplane and tandem wings at low Reynolds numbers," *Experiments in Fluids*, Vol. 56, No. 124, 2015, pp. 1-26.
https://doi.org/10.1007/s00348-015-1998-3
[20] Ekaterinaris, J. A., and Platzer, M. F., "Computational prediction of airfoil dynamic stall," *Progress in Aerospace Sciences*, Vol. 33, Iss. 11–12, 1998, pp. 759-846.
https://doi.org/10.1016/S0376-0421(97)00012-2
[21] Gursul, I., and Ho, C. M., "High aerodynamic loads on an airfoil submerged in an unsteady stream," *AIAA Journal*, Vol. 30, No. 4, 1992, pp. 1117-1119.
https://doi.org/10.2514/3.11034
[22] Gursul, I., Lin, H., and Ho, C. M., "Effects of time scales on lift of airfoils in an unsteady stream," *AIAA Journal*, Vol. 32, No. 4, 1994, pp.797–801.
https://doi.org/10.2514/3.12055
[23] Gursul, I., and Cleaver, D., "Plunging oscillations of airfoils and wings: Progress, opportunities, and challenges," *AIAA Journal*, Vol. 57, No. 9, 2019, pp. 3648-3665
https://doi.org/10.2514/1.J056655

[24] Chiereghin, N., Bull, S., Cleaver, D., and Gursul, I., "Three-dimensionality of leading-edge vortices on high aspect ratio plunging wings," *Physical Review Fluids*, Vol. 5, Iss. 6, 2020, p. 064701
https://doi.org/10.1103/PhysRevFluids.5.064701

[25] Qian, Y., Wang, Z., and Gursul, I., "Interaction of Quasi-Two-Dimensional Vortical Gusts with Airfoils, Unswept and Swept Wings" *AIAA Science and Technology Forum and Exposition (SciTech 2021)*, Music City Center Nashville, Tennessee, United States, 11–15 and 19–21 January 2021. AIAA 2021-1935.
https://doi.org/10.2514/6.2021-1935

[26] Barnes, C. J., and Visbal, M. R., "Computational Investigation of the Effect of Sweep on Parallel Vortical-Gust/Wing Interactions," *AIAA Science and Technology Forum and Exposition (SciTech 2019)*, San Diego, California, United States, 7-11 January 2019. AIAA 2019-0896.
https://doi.org/10.2514/6.2019-0896

[27] Cleaver, D., Wang, Z., and Gursul, I., "Investigation of High-Lift Mechanisms for a Flat-Plate Airfoil Undergoing Small-Amplitude Plunging Oscillations," *AIAA Journal*, Vol. 51, No. 4, 2013, pp. 968-980.
https://doi.org/10.2514/1.J052213

[28] Calderon, D. E., Wang, Z., and Gursul, I., "Lift-Enhancing Vortex Flows Generated by Plunging Rectangular Wings with Small Amplitude," *AIAA Journal*, Vol. 51, No. 4, 2013, pp. 2953-2964
https://doi.org/10.2514/1.J052600

[29] Wang, Z., and Gursul, I., "Unsteady characteristics of inlet vortices," *Experiments in Fluids*, Vol, 53, No. 4, 2012, pp. 1015-1032.
https://doi.org/10.1007/s00348-012-1340-2

[30] Moffat, R. J., "Describing the uncertainties in experimental results," *Experimental Thermal and Fluid Science*, Vol. 1, Iss. 1, 1988, pp. 3-17
https://doi.org/10.1016/0894-1777(88)90043-X

[31] Oudheusden, B. W., Scarano, F., Hinsberg, N. P., and Watt, D. W., "Phase-resolved characterization of vortex shedding in the near wake of a square-section cylinder at incidence," *Experiments in Fluids*, Vol. 39, No. 1, 2005, pp. 86-98.
https://doi.org/10.1007/s00348-005-0985-5

[32] Bendat, J., and Piersol, A., "Random data: analysis and measurement procedures," 4th ed., John Wiley & Sons, 2011, pp. 354-355.
https://doi.org/10.1002/9781118032428

[33] Hayakawa, M., and Hussain, F., "Three-dimensionality of organized structures in a plane turbulent wake," *Journal of Fluid Mechanics*, Vol. 206, 1989, pp. 375-404
https://doi.org/10.1017/S0022112089002338

[34] Turhan, B., Wang, Z., and Gursul, I., "Coherence of unsteady wake of periodically plunging airfoil," *Journal of Fluid Mechanics*, Vol. 938, 2022, pp. A14 1-32
https://doi.org/10.1017/jfm.2022.147

[35] Gutierrez-Castillo, P., Aguilar-Cabello, J., Alcalde-Morales, S., Parras, L., and del Pino, C., "On the lift curve slope for rectangular flat plate wings at moderate Reynolds number," *Journal of Wind Engineering and Industrial Aerodynamics*, Vol. 208, 2021, p.104459
https://doi.org/10.1016/j.jweia.2020.104459

[36] Phillips, N., Knowles, K., and Bomphrey, R. J., "The effect of aspect ratio on the leading-edge vortex over an insect-like flapping wing," *Bioinspir Biomim*, Vol. 10, No. 5, 2015, p. 056020.
https://doi.org/10.1088/1748-3190/10/5/056020